PHYSICAL REVIEW B VOLUME 24, NUMBER 10 15 NOVEMBER 1981

Dynamics of xenon-covered graphite slabs

E. de Rouffignac*
Instituto Mexicano del Petróleo, Investigacion Basica de Procesos, AP 14-805, Mexico, D. F., Mexico

G. P. Alldredge
Department of Physics, University of Missouri-Columbia, Columbia, Missouri 65211

F. W. de Wette
Department of Physics, University of Texas, Austin, Texas 78712

(Received 3 April 1981)

Following our earlier work [I; Phys. Rev. B 23, 4208 (1981)] on the dynamics of the graphite (0001) free surface, we present here a full dynamical calculation of a (0001) graphite slab with registered monolayers of xenon atoms adsorbed on its two surfaces. The xenon-xenon and xenon-carbon interactions are modeled with a Lennard-Jones potential, whereas the carbon-carbon interactions are described by the extended axially symmetric force-constant model introduced in I. Three doubly degenerate surface-mode branches are found which are associated with almost independent vibrations of the xenon layers in the potential field of the substrate. (However, for increasingly long wavelengths the substrate participates more and more in these vibrations which become the rigid-body translations for infinite wavelength.) Other surface modes involve mainly the underlying carbon slab and have their maximum amplitudes in the outer carbon layers. Density-of-states functions of the xenon-covered slabs have also been calculated, in connection with a future evaluation of the thermodynamic properties of this system.

I. INTRODUCTION

In a recent paper[1] (in the following to be referred to as I) we presented a full dynamical treatment of a graphite system with surfaces, more precisely, of a graphite slab of a finite but significant number of atomic layers, bounded by two free (0001) basal plane surfaces and infinitely extended in the directions parallel to the basal planes. As outlined in I, the motivation for this work is the increasing experimental interest in the study of a variety of physical properties of gases adsorbed on graphite surfaces. In the present paper we deal with the dynamics of the adsorbate-adsorbent system; in particular, we present a lattice-dynamical treatment of a graphite slab with a registered monolayer of xenon atoms adsorbed on its basal plane surfaces. To our knowledge this is the first study of an adsorbate-graphite system which takes full account of the dynamics of the graphite at a level of description approaching the standard of bulk lattice dynamics. This treatment goes beyond earlier works[2–4] which focus on more limited questions or more simplified models.

The fact that we consider a registered phase of adsorbed xenon atoms needs special mention. The question of the phase of the adsorbed xenon layer—gas, liquid, or solid—and the corresponding phase diagram has received considerable experimental and theoretical interest in recent years.[5] From a theoretical-computational point of view, an adsorbed monolayer in registry with the substrate is the most tractable system, amenable to straightforward computational treatment. Since this phase is believed to occur in at least part of the phase diagram at full monolayer coverage,[5] it is the system of choice to be treated first, and the present paper treats only this system.

A discussion of the thermodynamic properties of the bare graphite slab and of the xenon-covered slab, based on the dynamical studies of I and the present work, will be presented in a subsequent publication. In Secs. II and III we present, respectively, a formulation of the dynamics of the xenon-covered slab, and the results.

II. FORMULATION OF THE DYNAMICS OF THE XENON-COVERED GRAPHITE SLAB

In I we discussed the dynamics of bare graphite slabs with (0001) stress-free basal plane surfaces.

The calculations were carried out for 3-, 13-, and 21-layer slabs, but results were presented for the 21-layer slab only. The addition of a registered monolayer of xenon atoms adsorbed on the surfaces of the slab increases the computational memory requirements to such an extent that a 21-layer substrate calculation becomes unfeasible. A calculation of xenon adsorbed on a 13-layer slab appeared to be the best compromise between, on the one hand, reducing the undesired effects of an extremely-thin-film calculation and, on the other hand, the restrictions imposed by the memory capacity of the available computers.

The registered monolayer of xenon adsorbed on the (0001) plane of graphite has a 30° $\sqrt{3}\times\sqrt{3}$ structure as depicted in Fig. 1. This means that the planar cross section of the primitive cell for the xenon-covered graphite slab (XGS) (which extends through the entire thickness of the slab) is rotated by 30° with respect to the primitive cell for the bare graphite slab (BGS), and that the primitive translation vectors of the XGS are a factor $\sqrt{3}$ larger than those of the BGS. Thus the XGS unit cell contains one xenon atom on each slab surface and six carbon atoms in each graphite layer (see Fig. 2). A 15-layer XGS (13 graphite layers and 2 xenon layers) contains 78 carbon atoms and 2 xenon atoms per slab unit cell; this means that we will have to work with a 240×240 (complex) dynamical matrix. Since the memory requirement to store the elements of such a matrix approached the available memory of the CDC 6600, we had to utilize group-theoretical methods to block-diagonalize the dynamical matrix, in order to reduce the size of the matrices to be stored in memory and to significantly speed up the calculation.

As in the BGS calculations (cf. I), the carbon-carbon interactions are treated in a modification of the "axially-symmetric" pairwise interaction model as used by Nicklow, Wakabayashi, and Smith.[6] As in Suzanne *et al.*[3(a)] and Coulomb and Masri,[3(c)] we describe the xenon-xenon and xenon-carbon pair interactions by Lennard-Jones potentials,

$$\phi(r)=4\epsilon[(\sigma/r)^{12}-(\sigma/r)^{6}]\ , \tag{1}$$

where r is the distance between the interacting atoms, and ϵ and σ are the potential parameters. The values of ϵ and σ for the xenon-xenon and xenon-carbon interactions were obtained from the

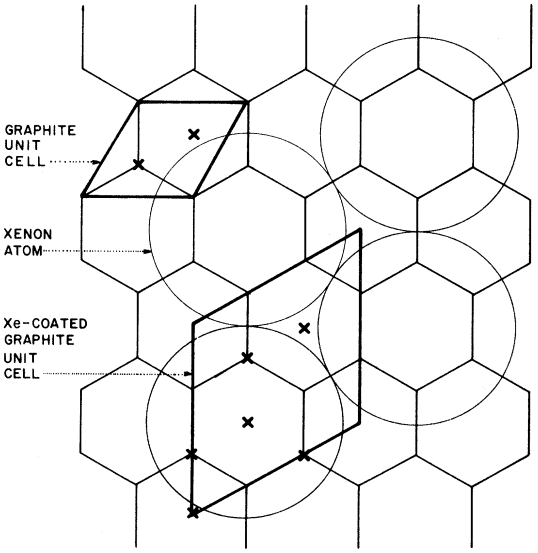

FIG. 1. Xenon epitaxially located on the graphite (0001) surface in a (30° $\sqrt{3}\times\sqrt{3}$) overlayer structure. Vertices of the hexagonal net mark carbon atoms in the first graphite plane, × marks carbon atoms in the second graphite plane.

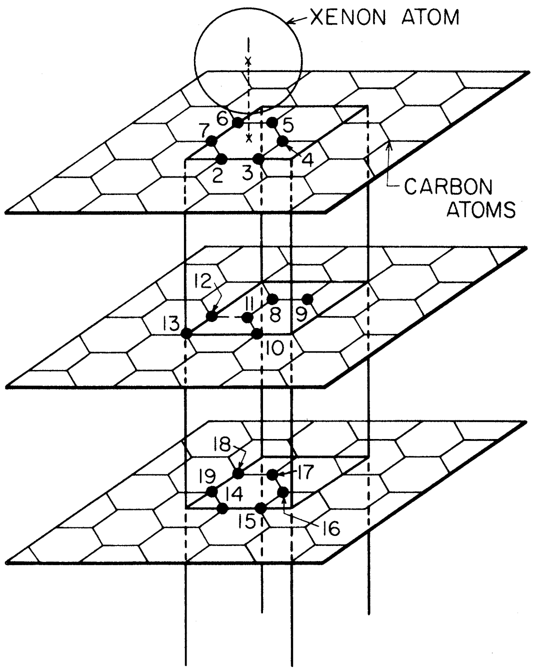

FIG. 2. Slab (primitive) unit cell of xenon adsorbed on the (0001) surface of a graphite slab. The xenon atom is located over the center of the numbered graphite hexagon. The carbon atoms in the unit cell are numbered sequentially, beginning with the xenon atom on top as number 1. The xenon atom on the bottom surface of the slab will be number 80 for a 13-layer substrate graphite slab.

work of Crowell and Steele.[7]

The carbon–carbon distances in the XGS are the same as those used in the BGS (cf. I). The equilibrium distance z_0 of the xenon atoms with respect to the outer graphite layer was determined by minimization of the potential energy of the xenon atom with respect to z_0. This potential energy included the interaction of a xenon atom with all carbon atoms contained in a sphere centered on the xenon atom, with a radius extending to halfway between the 7th and 8th graphite planes, measured from the xenon atom. The equilibrium distance z_0, as well as the potential parameters ϵ and σ, are given in Table I.

Since the primitive cell of the XGS has a cross-sectional area which is 3 times as large as that of the primitive cell of the BGS, the two-dimensional (2D) surface Brillouin zone (SBZ) of the XGS has an area one third the size of the SBZ of the BGS; both SBZ's are shown in Fig. 3, where the 30° difference in orientation is exhibited, and the mapping of the BGS zone into the XGS zone is indicated.

In comparing the calculated frequencies of the 15-layer XGS with those of the 13-layer BGS, one will get for the XGS for each 2D wave vector $\bar{q}$, not only six extra frequencies resulting from the presence of the two xenon atoms, but in addition 3 times as many frequencies as in the BGS case because of the increased size of the SBZ. This can be understood by examination of Fig. 3. The reciprocal-lattice translations of the XGS map the two shaded areas of the BGS-SBZ, lying outside the XGS-SBZ, onto the irreducible element $\bar{\Gamma}\bar{M}_R\bar{K}_R$ of the XGS-SBZ. In a similar fashion, the entire area of the BGS-SBZ outside the XGS-SBZ can be mapped back onto the XGS-SBZ. As a consequence, diagonalization of the dynamical matrix for a wave vector $\bar{q}$ of the XGS-SBZ gives rise to a set of frequencies corresponding approximately to those obtained for three wave vectors $\bar{q}$ in the BGS-SBZ.

TABLE I. Interatomic potential parameters and equilibrium distance for xenon adsorbed on graphite.

	Xe-Xe	Xe-C
σ (Å)[a]	3.97	3.69
ϵ (10^{-14} erg)[a]	3.15	1.08
	$z_0=3.64$ Å	

[a] Potential parameters derived from Crowell and Steele, Ref. 7.

A. Block diagonalization

As mentioned above, the much greater size of the dynamical matrix for the XGS case over that for the BGS case requires the use of some symmetry reduction of the dynamical matrix. Because most of our calculational effort would be at general points of the SBZ, the only symmetry generally available is that of C_{1h} (for reflection σ_h in the median plane of the slab). In effect then, we apply a unitary transformation $S(\bar{q})$ on the dynamical matrix $D(\bar{q})$, such that[8,9]

$$S(\bar{q})D(\bar{q})S^{-1}(\bar{q})=\underline{D}(\bar{q}) \tag{2}$$

where

$$\underline{D}(\bar{q})=\begin{bmatrix} \underline{D}^{(+)}(\bar{q}) & 0 \\ 0 & \underline{D}^{(-)}(\bar{q}) \end{bmatrix} . \tag{3}$$

In Eq. (3) we have already specialized to the special case of reduction under C_{1h}; hence $\underline{D}^{(+)}(\bar{q})$ is the block transforming according to the even irreducible representation of C_{1h} and $\underline{D}^{(-)}(\bar{q})$ is that for the odd irreducible representation. For the 15-layer XGS, $\underline{D}^{(+)}$ is of dimension 123

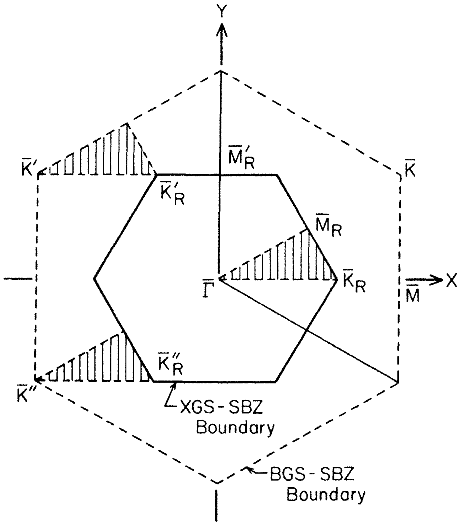

FIG. 3. Surface Brillouin zones. The large hexagon is the SBZ of the bare slab (BGS), the small hexagon is the SBZ for the xenon-covered slab (XGS). The outer portions of the BGS which map into the irreducible element of the XGS are shown as shaded, with $\bar{K}'$ and $\bar{K}''$ as images of $\bar{\Gamma}$.

$(=3+3\times6\times[(13-1)/2]+(3-1)\times6)$, and $\underline{D}^{(-)}$ is of dimension 117 $(=3+3\times6\times[(13-1)/2]+(3-2)\times6)$. For further details on the implementation of this reduction, see Ref. 10.

B. Diagonalization of the dynamical matrix

Even after the dynamical matrix has been reduced under the C_{1h} symmetry for all wave vectors $\bar{q}$, practical considerations require a further division of the diagonalization procedures into two subcases: (1) For a relatively small set of wave vectors, one wants from the outset a solution for the complete eigensystem (both the eigenvalues *and* the eigenvectors); (2) for a much larger set of wave vectors, for many purposes one can settle for just the eigenvalues. The first case is much more demanding of both computer memory and time. Hence, for the purposes of the present paper, the complete eigensystems were produced only along a single edge of the irreducible part of the SBZ (ISBZ), $\bar{\Gamma}\bar{K}_R$.

Except for the addition of the symmetry reduction for C_{1h}, the computational procedures for diagonalizing the diagonal matrices were the same as were used for the BGS case of I. Because the memory requirements for the solution of the complete eigensystem approached maximum memory available on the CDC 6600 of the University of Texas at Austin, all XGS calculations were carried out on the Univac-1106 computer of the Instituto Mexicano del Petróleo in Mexico City. The calculation of the complete eigensystem at a given $\bar{q}$ point required 130 k (decimal) words of main storage and 25 min of CPU time on the Univac-1106. Consequently, 10 h of Univac-1106 time were required to obtain a set of dispersion curves (and associated eigenvectors) for 21 wave vectors along a given edge of the ISBZ.

III. RESULTS

A. Phonon dispersion curves

Because of the heavy requirement of computer time for these calculations, so far we have only calculated dispersion curves for 21 equally spaced wave vectors $\bar{q}$ chosen along the boundary $\bar{\Gamma}\bar{K}_R$ of the ISBZ. As we discussed earlier, for each wave vector in the ISBZ of the XGS, we get 3 times as many frequencies as for a wave vector in the ISBZ of the BGS, plus six additional frequencies. In particular, sampling along the segment $\bar{\Gamma}\bar{K}_R$ of the XGS-SBZ gives frequencies for the substrate-dominated motions which are in close correspondence with the 13-layer slab frequencies along the segments $\bar{\Gamma}\bar{K}_R$, $\bar{K}'\bar{K}_R'$, and $\bar{K}''\bar{K}_R''$ of the BGS-SBZ (Fig. 3).

The dispersion curves for frequencies along the segment $\bar{\Gamma}\bar{K}_R$ of the XGS-ISBZ are plotted in Fig. 4. For comparison we present the BGS results for wave vectors along $\bar{\Gamma}\bar{M}$ of the BGS-SBZ in Fig. 5. The labeled dispersion curves in Fig. 4 are in close correspondence with those for the segment $\bar{\Gamma}\bar{K}_R$ $(=\frac{2}{3}\bar{\Gamma}\bar{M})$ in Fig. 5. The six bulklike bands labeled 1 through 6 in both figures are (basically) the same bands for the $\frac{2}{3}\bar{\Gamma}\bar{M}$ segment. The other bulklike bands in Fig. 4 do not appear in Fig. 5, because, except for the very lowest band associated with the xenon modes, they correspond to frequencies along the segments $\bar{K}'\bar{K}_R'$ and $\bar{K}''\bar{K}_R''$ in the BGS-ISBZ; note that the bare-graphite bands along these two segments are degenerate with each other. The bands in Fig. 5 along $\bar{K}_R\bar{M}$ correspond to some of the XGS bands along $\bar{K}_R\bar{M}_R$ (not shown here).

B. Surface modes

The low-lying band in Fig. 4, which consists of three dispersion curves and which is well separated from band 1 over most of the XGS-SBZ, represents *surface modes* (for a definition we refer to I). It has been shown, for example, by Alldredge *et al.*[11], that when a layer of heavy atoms is adsorbed on a

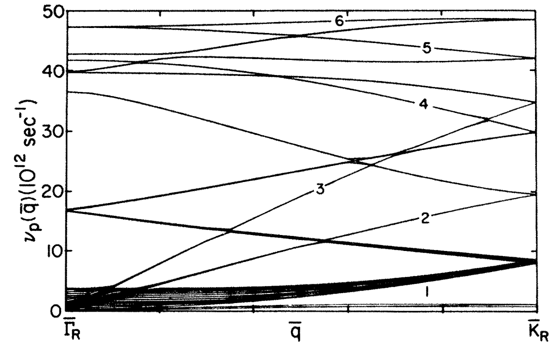

FIG. 4. Dispersion curves for the XGS for wave vectors along the segment $\bar{\Gamma}_R\bar{K}_R$ of the irreducible SBZ. The numbered curves correspond to those of the BGS out to $\bar{K}_R$ in Fig. 5.

substrate consisting of lighter atoms, one set of surface modes will have frequencies which, in general, lie below the lowest bulk bands of the adsorbent system. For these particular surface modes it is found that, well away from the center of the SBZ and over most of the SBZ, the main vibrational amplitude occurs for the adsorbed xenon atom, with the mode amplitude for substrate (carbon) atoms diminishing rapidly away from the surface.

In Fig. 6 we give an expanded view of the low-frequency region of Fig. 4. The three low-lying modes are approximately doubly degenerate, representing the near degeneracy of the xenon-dominated motion on the top and bottom surfaces of the slab. Close to the zone center $\bar{\Gamma}_R$, these modes exhibit some hybridization with the bottom of the lowest substrate band (which is a common occurrence in situations like this) and their degeneracy is visibly split. The surface-mode character of these modes is determined from an examination of the polarization vectors $\vec{\xi}(\kappa;\bar{q}p)$ for fixed 2D wave vector $\bar{q}$ and given polarization p; κ labels the atoms in the slab unit cell. In practice we decompose the index κ into two indices (m,i), where m labels the atomic plane and i the atoms in each plane (for details, we refer to I). Then, for fixed $\bar{q}$ and p we examine the quantity

$$|\vec{\xi}(m)|^2 = |\xi_x(m)|^2 + |\xi_y(m)|^2 + |\xi_z(m)|^2 . \quad (4)$$

For the 15-layer XGS, $m=1$ and 15 correspond, respectively, to the top and bottom layers consisting solely of the xenon atoms, $m=2$ and 14 correspond to the outermost graphite layers, and so on. [Absence of an atom index means the average of $|\xi_\alpha(m,i)|^2$ over all atoms i in layer m.]

For wave vectors along $\bar{\Gamma}\bar{K}_R$, the sagittal plane (the plane defined by the surface normal and the wave vector) is a plane of mirror symmetry. Hence, the modes can be characterized as either (1) SH (shear-horizontal, i.e., linear polarization normal to the sagittal plane) or (2) SP (elliptical polarization with the plane of the ellipse coinciding with the sagittal plane). The SP modes usually can be further subcategorized in a qualitative sense as either (a) $SP_\perp$, which has the largest component of the semimajor axis along the surface normal, and (b) $SP_{\parallel}$, which has the largest semimajor axis component parallel to the surface (hence parallel to the 2D wave vector). (Of course, when the sagittal plane is no longer a mirror plane, e.g., along $\bar{\Gamma}\bar{M}_R$, the SH or SP character is no longer strictly held; however, usually modes can still be roughly characterized as SH, $SP_\perp$, or $SP_{\parallel}$.)

The low-lying, predominantly Xe-motion modes in Fig. 6 can thus be characterized as follows. The band that is highest in frequency over most of $\bar{\Gamma}\bar{K}_R$ is of $SP_{\parallel}$ character, approximating a longitudinal (compressional) wave in the Xe monolayer. The band that is fairly flat over the outer two-thirds of $\bar{\Gamma}\bar{K}_R$ is of $SP_\perp$ character. It approximates the transverse wave of the monolayer that is modified by the near-static vertical force field of the substrate; as expected, it is the monolayer mode

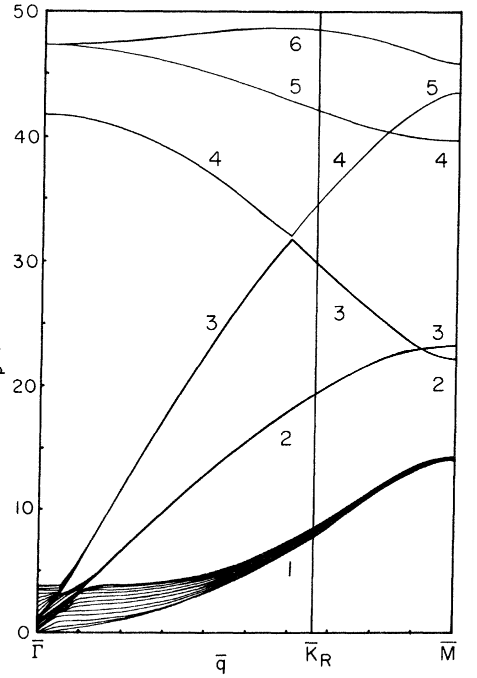

FIG. 5. Dispersion curves for the BGS, for wave vectors along the segment $\bar{\Gamma}\bar{M}$. The segment $\bar{\Gamma}\bar{K}_R$ corresponds to the segment $\bar{\Gamma}_R\bar{K}_R$ of Fig. 4 ($\bar{\Gamma}_R\bar{K}_R=\frac{2}{3}\bar{\Gamma}\bar{M}$).

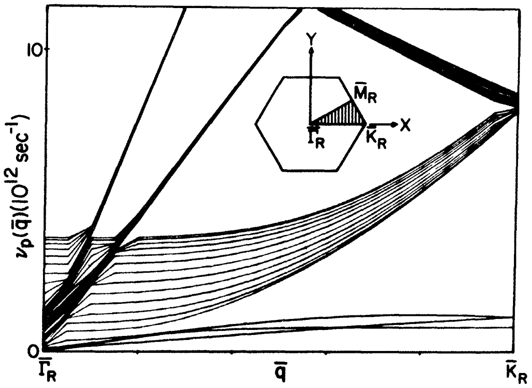

FIG. 6. Expanded view of XGS dispersion curves along the segment $\bar{\Gamma}_R\bar{K}_R$ (cf. Fig. 4).

most strongly coupled to the substrate. The band which is fairly low at small $\bar{q}$, then rises to cross the $SP_\perp$ band at about $0.64\overline{\Gamma K}_R$ and meets the $SP_\parallel$ band at $\bar{K}_R$, is of SH character; it approximates that monolayer transverse wave which is only slightly modified by the lateral forces of the substrate, except at the longest wavelengths. (Note: we have spoken here of "bands" of SP and SH character because the eye tends to follow the path of such dynamical character along a complex of dispersion curves. Strictly speaking, however, the most consistent scheme of indexing bands over the entire SBZ is in terms of strictly increasing frequency at each $\bar{q}$ in the SBZ; we adhere to this latter convention when we characterize a band by a numerical index.)

In Fig. 7 we display on a semilogarithmic scale the "attenuation curves," the *physical* square displacement $|\vec{u}(m)|^2 = M_m^{-1}|\vec{\xi}(m)|^2$ versus m, for the three low-lying surface modes Xe_1, Xe_2, and Xe_3, as well as for the three lowest-frequency graphite slab surface modes which still exhibit detectable surface localization in the presence of the xenon, all at wave vector $\bar{q} = \frac{11}{20}\overline{\Gamma K}_R$. It is seen that for Xe_1, Xe_2, and Xe_3 the mode amplitude is mainly confined to the top xenon layer ($m = 1$), with the amplitude in the first underlying graphite layer being down by almost 2 orders of magnitude for Xe_2, and by several orders of magnitude for Xe_1 and Xe_3. Thus, in these modes at this large wave vector, the layer vibrates practically independent of the substrate but in the static potential field of the substrate atoms. A measure of the degree of participation of the substrate in this motion is given by Xe_2, which as the $SP_\perp$ mode at this wave vector has the greatest coupling to the substrate. At the relatively large wave vector of Fig. 7, mode Xe_2 has only about 0.1% participation by the outermost carbon plane. However, the coupling to substrate motion increases with increasing wavelength (decreasing $\bar{q}$) and the bands Xe_1, Xe_2, and Xe_3 evolve into the three rigid-body translations as $\bar{q} \to 0$. This fact raises some question concerning the validity of the "frozen substrate" assumption made by Coulomb and Masri[3(c)] for their two-layer model of the xenon-graphite system; we plan to address this question more directly in future work. We finally point out the near linear behavior of these semilogarithmic attenuation curves from the graphite surface layer ($m = 2$) inward. This indicates that at this wave vector the variation with depth of the amplitudes of each of the modes Xe_1, Xe_2, and Xe_3 is dominated by a single decaying exponential in the substrate; i.e., $\xi(m) \propto \exp(-\alpha mc)$, where $\alpha = \mathrm{Im}(q_z)$ (different for each of the modes) and c is the fundamental interplanar distance. The evanescent waves giving rise to this behavior come from the complex band structure of graphite, and because in the present case the modes are so much more removed in frequency from the associated bulk band edges, the imaginary parts of the q_z have gotten much larger than those seen for bare graphite (Ref. 1).

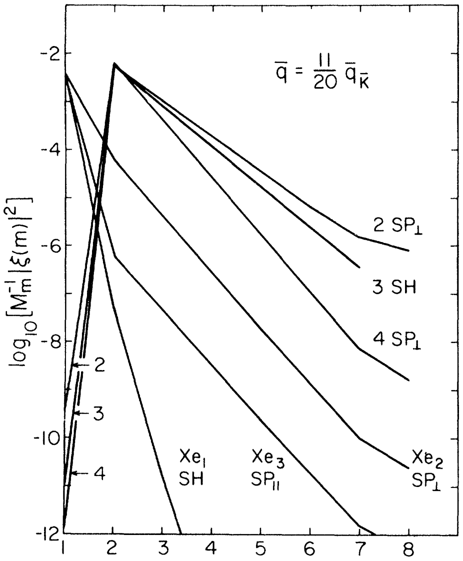

FIG. 7. Attentuation with depth of the physical square amplitude $|\vec{u}(m)|^2 = M_m^{-1}|\vec{\xi}(m)|^2$ of selected vibrational modes of the XGS at $\bar{q} = \frac{11}{20}\bar{q}_{\bar{K}_R}$, on a semilogarithmic scale. [M_1 is the mass of a xenon atom, M_m ($m > 1$) that of a carbon atom]. The curves labeled Xe_1, Xe_2, and Xe_3 refer to modes in which the main amplitude is found for the adsorbed xenon atoms. The other three curves pertain to surface modes of the graphite substrate, at frequencies 24.07 (2 $SP_\perp$), 26.37 (3 SH), and 37.70 THz (4 $SP_\perp$).

The other three attenuation curves displayed in Fig. 7 represent the lowest-lying substrate surface modes that still exist at this wave vector in the presence of the xenon overlayer. These modes are at 24.07, 26.37, and 37.70 THz, and are associated most directly with bands 2, 3, and 4 of the BGS band structure (see Fig. 5 and Ref. 1). The modes at 24.07 and 26.37 THz are associated with $\bar{q}$ points ($\frac{11}{20}$) along $\bar{K}'\bar{K}_R'$ and $\bar{K}''\bar{K}_R''$ in Fig. 3, so they are approximately fourfold degenerate to a rather high precision; the presence of the xenon overlayer prevents the exact degeneracy between the frequencies of pairs of modes of the same irreducible representation of C_{1h} (σ_h symmetry)—the splitting is about 2 parts in 10^4, whereas the splitting between modes of opposite σ_h symmetry (because of the finite thickness of the substrate) is about one order of magnitude smaller. The modes at 37.70 THz are associated with $\bar{q}=(\frac{11}{20})\bar{\Gamma}\bar{K}_R$ in Fig. 3, so the only near degeneracy they exhibit is just the double degeneracy between modes of opposite σ_h symmetry. All substrate surface modes below 24 THz at $\bar{q}=(\frac{11}{20})\bar{\Gamma}\bar{K}_R$ in the XGS-SBZ have been extinguished by the presence of the xenon overlayer; the extinguished modes include not only those of bands 1, 2, and 3 at $\bar{K}_R$ in Fig. 5, but also the large wave-vector modes (along $\bar{K}'\bar{K}_R'$ and $\bar{K}''\bar{K}_R''$ in Fig. 3) at about 11 THz. Notice that the "substrate" surface modes in Fig. 7 still exhibit a decay of the amplitudes that is practically pure exponential in nature, but with different decay constants α for each of the modes.

The nature of the interaction between xenon atom motions and those of the graphite substrate can be further elucidated with the aid of Fig. 8,

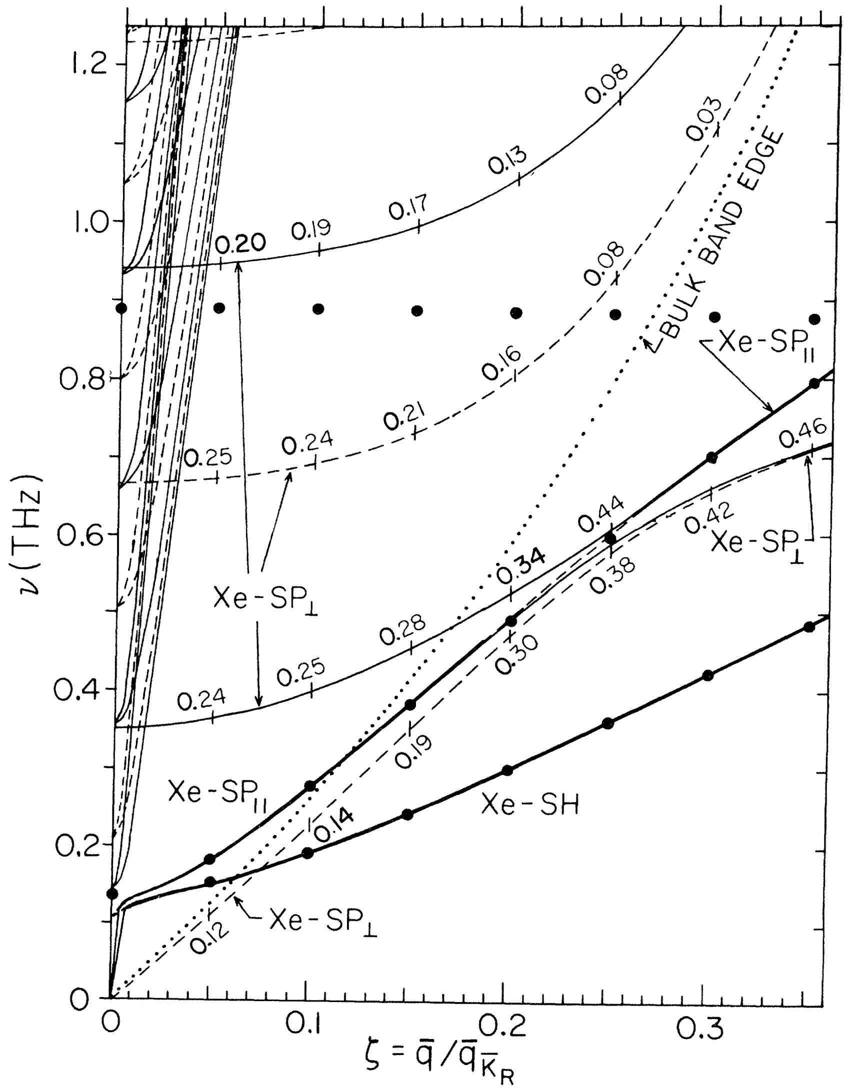

FIG. 8. Low-frequency, small $\bar{q}$ enlargement of the XGS dispersion curves. Light solid and dashed lines are, respectively, the XGS curves for the even and odd irreducible representation of C_{1h}. Where pairs of surface modes are essentially degenerate between the even and odd irreducible representations, the curves are made into heavy solid lines. The value of $|\vec{\xi}(\mathrm{Xe})|^2$ is given at vertical hash marks crossing certain dispersion curves at $\zeta=0.05$, 0.1, 0.15, 0.20, 0.25, 0.30, and 0.35. The heavy dots indicate the Xe dispersion curves when the substrate is "static" (i.e., $M_{\text{carbon}}=10^{26}$ amu).

which shows an enlargement of the low-frequency, small-wave-vector portion of the XGS dispersion curves. The lowest edge of the graphite bulk bands is represented by the dotted line, which is actually the lowest BGS frequency (paper I notes the very close proximity of the BGS surface modes to the associated bulk bands). At $\zeta < 0.01$, both the Xe-SH and Xe-$SP_{\|}$ modes "cross" the sharply rising graphite bulk subbands, where there is a strong interaction over a range of about 0.02 THz around about 0.12 THz. From $\zeta > 0.01$ to the SBZ boundary, the Xe-SH branch has almost all the normal mode amplitude in the Xe atoms; i.e., for this pair of modes $|\vec{\xi}(\mathrm{Xe})|^2 = 0.500$ to better than 0.1%. [Note that with our slab eigenvectors normalized to unity, a uniform translation of our Xe-graphite slab has $|\vec{\xi}(\mathrm{Xe})|^2 = 0.10954$ and $|\vec{\xi}(\mathrm{C})|^2 = 0.01001$, which takes into account the mass weighting of the eigenvector components.] Near $\zeta = 0.23$, the Xe-$SP_{\|}$ branch "crosses" the Xe-$SP_{\perp}$ branch, and in this 13-layer substrate slab the strong interaction of the Xe-$SP_{\perp}$ branch with the lowest $SP_{\perp}$ bulk band of graphite appears to induce a noticeable amount of additional splitting of the Xe-$SP_{\|}$ branch in the neighborhood of the crossing. Aside from these noted interactions, the Xe-$SP_{\|}$ and Xe-SH motions appear to be decoupled from the graphite motions to a rather high precision; where the hash marks have been omitted from the heavy curves in Fig. 8, $|\vec{\xi}(\mathrm{Xe})|^2 = 0.50$ to better than 1%. The decoupling of the Xe-SH branch along $\overline{\Gamma}\overline{K}_R$ is, of course, an exact symmetry-enforced decoupling (except below $\zeta < 0.01$ where there are graphite SH bulk modes), but one would expect the coupling to remain very weak away from the $\overline{\Gamma}\overline{K}_R$ direction because there will be still very little z amplitude in the SH modes and very little SH component in the bulk SP band. For the Xe-$SP_{\|}$ branch there is a small component of z amplitude even along $\overline{\Gamma}\overline{K}_R$, but it is so small that to better than 1% the even and odd Xe-$SP_{\|}$ modes are degenerate and contain all the amplitude in the Xe atoms, even within the $SP_{\perp}$ bulk band of graphite.

On the other hand, Fig. 8 illustrates the very strong interaction of Xe-$SP_{\perp}$ branch with the $SP_{\perp}$ bulk band of graphite. While a normal mode calculation of a sample of finite thickness is not the most direct way of discussing strongly coupled resonant states, it can yield qualitative features. For example, in Fig. 8 we see that at $\zeta = 0.05$ the lowest even Xe-$SP_{\perp}$ curve (at about 0.36 THz) has $|\vec{\xi}(\mathrm{Xe})|^2 = 0.24$, and the second-lowest odd Xe-$SP_{\perp}$ curve (at about 0.67 THz) has $|\vec{\xi}(\mathrm{Xe})|^2 = 0.25$. They both lie within the $SP_{\perp}$ bulk band of graphite, so that much of the loss of amplitude from the Xe atoms goes into bulklike motions of the graphite substrate. From this distribution of Xe amplitudes and from the general trend of the Xe-$SP_{\perp}$ branch outside the graphite bulk continuum, one can estimate that the peak of the spectral weight for the Xe-$SP_{\perp}$ "resonance" would be at about 0.55 THz at $\zeta = 0$. The rather broad distribution of fairly large values of $|\vec{\xi}(\mathrm{Xe})|^2$ over frequency out to about $\zeta = 0.17$ indicates that the resonance is a fairly broad one. Note that the lowest odd Xe-$SP_{\perp}$ curve lies below the graphite bulk band everywhere; as $\zeta \to 0$, it transforms into the flexural mode of a plate, and by $\zeta = 0.05$, $|\vec{\xi}(\mathrm{Xe})|^2 = 0.12$, which is almost the value 0.10954 characteristic of uniform displacement of this Xe-graphite slab.

In Fig. 8 we also give for comparison the dispersion curves (denoted by the heavy dots) for xenon coupled to a static substrate, but otherwise described by the interactions of Table I. The static substrate has been simulated in our slab dynamics calculations by setting the mass of the carbon atoms in the substrate to a very large value ($M_{\mathrm{carbon}} = 10^{26}$ amu is the value used, but the results for the Xe frequencies are insensitive to the particular value so long as it is large enough). It is evident that the Xe-SH and the Xe-$SP_{\|}$ modes are largely unaffected by dynamic coupling to the substrate, except for a small region of $\zeta \lesssim 0.02$. On the other hand, the Xe-$SP_{\perp}$ modes change greatly when a dynamic substrate is included. On the static substrate, the Xe-$SP_{\perp}$ branch is very flat, starting at 0.882 THz at $\zeta = 0$ and decreasing to 0.869 THz at $\zeta = 0.35$ in Fig. 8. When the substrate is dynamic, this branch becomes the broad resonance in the graphite bulk band described above, and its center has been shifted to a considerably lower frequency. Even outside the graphite bulk band, the Xe-$SP_{\perp}$ band is significantly lowered from the static substrate value. These shifts to lower frequencies brought about by the dynamic substrate may be expected to have important consequences for thermally averaged quantities.

C. Slab frequency distribution

The slab frequency distribution $g^{\mathrm{slab}}(\nu)$ of the XGS is of importance, among other reasons, for the calculation of thermodynamic properties of the xenon-covered slab; thermodynamic properties will be discussed in a subsequent paper, but it is useful to round out the present discussion of the dynamics by a summary of the $g^{\text{slab}}(\nu)$ result. Of particular interest are any features in $g^{\text{slab}}(\nu)$ which result from the presence of the adsorbed xenon layer; to reveal these we compare the $g^{\text{slab}}(\nu)$ for the XGS with the same quantity for the BGS.

We evaluated $g^{\text{slab}}(\nu)$ for the XGS by a root sampling of frequencies throughout the ISBZ of the XGS. In I we discussed the difficulties in evaluating $g^{\text{slab}}(\nu)$ when a limited of sampling points are available. In Fig. 9 we display the functions $g^{\text{slab}}(\nu)$ for both the BGS [Fig. 9(a)] and the XGS [Fig. 9(b)]. The root sampling for both $g(\nu)$ distributions in Fig. 9 was based on a uniform mesh of 210 points in the irreducible element of the XGS, corresponding to a division of $\overline{\Gamma K}_R$ and $\overline{\Gamma M}_R$ into twenty intervals each. The calculation for the BGS [Fig. 9(a)] was done for exactly the same 13-layer graphite slab as for the XGS [Fig. 9(b)], except the xenon-xenon and xenon-graphite interactions were removed; hence the two calculations sample the XGS-SBZ at exactly the same $\vec{q}$ values. Despite the heavy demand of computer time by these calculations, there is still substantial "noise" in the $g(\nu)$ of Figs. 9(a) and 9(b) because of the extremes of narrowness of the bands, wide separations between bands, and the small histogram channel width. (Note, however, that the noise pattern is essentially the same in the two figures because the sample points were exactly the same). The very prominent low-frequency peaks in Fig. 9(b) around 1 THz [absent in Fig. 9(a)] arise from the adsorbate modes Xe_1, Xe_2, and Xe_3. They are well resolved here because of their relative flatness and limited spread; the large peak at about 0.8 THz arises primarily from the $\text{SP}_\perp$-character Xe-dominated modes, while the smaller peak at about 1.25 THz is due to the largely $\text{SP}_\parallel$ character of Xe_3 at large frequency over most of the XGS-SBZ. A more detailed discussion of the functions $g^{\text{slab}}(\nu)$ must await a subsequent paper which will deal with the thermodynamic properties of the xenon-covered graphite slab.

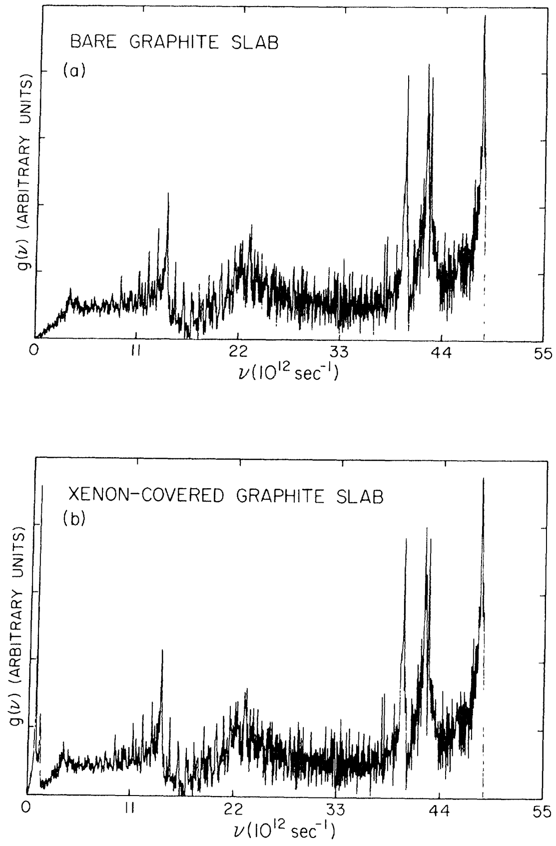

FIG. 9. (a) Slab frequency distribution $g^{\text{slab}}(\nu)$ for a 13-layer bare graphite slab. (b) Slab frequency distribution $g^{\text{slab}}(\nu)$ for a xenon-covered graphite slab of 15 layers (including the top and bottom xenon layers). The histogram channel width is 0.05 THz in both plots.

ACKNOWLEDGMENT

We thank Dr. Javier Tejeda Ruiz for valuable assistance in implementing the computations at the Instituto Mexicano del Petróleo and Dr. B. M. Firey for useful comments on the extended axially symmetric model used here. We acknowledge research support by the National Science Foundation under Grant No. DMR 78-10309 and the Robert A. Welch Foundation (F. W. de W.), and by the Consejo Nacional de Ciencia y Technologia (E. de R.). We also acknowledge computing support of the University of Missouri Computer Network, where the detailed calculations summarized in Fig. 8 were performed.

---

*Present address: Shell Development Co., Bellaire Research Center, Houston, TX 77001.

[1] E. de Rouffignac, G. P. Alldredge, and F. W. de Wette, Phys. Rev. B 23, 4208 (1981).

[2] (a) G. Albinet, J. P. Biberian, and M. Bienfait, Phys. Rev. B 3, 2015 (1971); (b) J. P. Biberian, M. Bienfait, and J. B. Theeten, Acta Crystallogr. Sect. A 29, 221 (1973). These works use a simple first-neighbors model (with five force constants related to the elastic constants) to discuss primarily the mean-square am-

plitudes of bulk and surface vibrations of graphite. This model underestimates by some twenty percent the low-lying LO branch along the [0001] direction which corresponds to opposing motion of adjacent (0001) planes [see Ref. 2(b)].

[3](a) J. Suzanne, P. Masri, and M. Bienfait, Surf. Sci. 43, 441 (1974); Jpn. J. Appl. Phys. Suppl. 2, part 2, 295 (1974); (b) J. P. Coulomb, J. Suzanne, M. Bienfait, and P. Masri, Solid State Commun. 15, 1585 (1974); (c) J. P. Coulomb and P. Masri, Solid State Commun. 15, 1623 (1974). These works examine various aspects (especially surface entropy and mean-square vibrational amplitudes) of Xe and Kr adsorbed on graphite, using a simple force-constant model restricted to nearest-neighbor interactions. Papers (a) and (b) keep the graphite substrate static, while (c) examines a dynamically coupled two-plane model—a single dynamic plane of graphite bearing an adsorbed monolayer.

[4] A. D. Novaco and J. P. McTague, Phys. Rev. B 20, 2469 (1979).

[5] See, for example, the review article: J. A. Venables and P. S. Schabes-Retchkiman, J. Phys. (Paris) Suppl. C4, 38, 105 (1977).

[6] R. Nicklow, N. Wakabayashi, and H. G. Smith, Phys. Rev. B 5, 4951 (1972).

[7] A. D. Crowell and R. B. Steele, J. Chem Phys. 34, 1347 (1961).

[8] A. A. Maradudin, E. W. Montroll, G. M. Weiss, and I. P. Ipatova, *Theory of Lattice Dynamics in the Harmonic Approximation,* 2nd ed. (Academic, New York, 1971), Chap. III.

[9] A. A. Maradudin and S. H. Vosko, Rev. Mod. Phys. 40, 1 (1968).

[10] E. P. de Rouffignac, Ph.D. thesis, University of Texas at Austin, 1979 (unpublished). Available from University Microfilms Inc., P. O. Box 1764, Ann Arbor, Mich. 48106, Order No. 7920103.

[11] G. P. Alldredge, R. E. Allen, and F. W. de Wette, Phys. Rev. B 4, 1682 (1971).